# Impact of a scale-aware convective parameterization scheme on the simulation of convective cells related heavy rainfall in South Korea

**Haerin Park[1], Gayoung Kim[1], Dong-Hyun Cha[1], Eun-Chul Chang[2], Joowan Kim[2], Sang-Hun Park[3], Dong-Kyou Lee[4]**

[1] Department of Urban & Environmental Engineering, Ulsan National Institute of Science and Technology, Ulsan, South Korea

[2] Department of Atmospheric Sciences, Kongju National University, Kongju, South Korea

[3] Department of Atmospheric Sciences, Yonsei University, Seoul, South Korea

[4] School of Earth and Environmental Sciences, Seoul National University, Seoul, South Korea

Corresponding author: Dong-Hyun Cha (dhcha@unist.ac.kr)

†School of Urban and Environmental Engineering

Ulsan National Institute of Science & Technology (UNIST)

50 UNIST-gil, Ulju-gun, Ulsan 689-798, South Korea

Office) +82-52-217-2828, Fax) +82-52-217-2809

**Key Points:**

- We investigated the impact of the scale-aware convective parameterization scheme across the gray-zone using the WRF model.
- The scale-aware CPS improved simulated convective cells related to rainfall by properly removing atmospheric instability in the gray-zone.
- CAPE timescale and entrainment rate modulated in the scale-aware MSKF are the key parameters for the improved rainfall simulation in the gray-zone.

## Abstract

This study investigates the impact of the scale-aware convective parameterization scheme (CPS) on convective cells related to simulation of heavy precipitation across the gray-zone using the Weather Research and Forecasting (WRF) model. We select the Kain-Fritsch (KF) and Multi-scale Kain-Fritsch (MSKF) schemes as non-scale-aware and scale-aware CPSs, respectively. The MSKF scheme uses a scale-aware parameter that modulates the convective available potential energy (CAPE) timescale and entrainment process in the KF scheme as a function of the horizontal grid spacing. This study shows that simulation of convection only with grid-scale process microphysics parameterization scheme (MPS) (i.e., explicitly resolved) causes an unreasonably overestimated and erroneous location of precipitation in the gray-zone because convection and atmospheric instability could not properly be triggered and reduced. Contrarily, the CPS without scale-awareness in the gray-zone exaggerates the convection and distorts synoptic fields, leading to the erroneous simulation of heavy precipitation at high resolution. Contrastingly, the MSKF scheme with scale-awareness improves simulated convective cells related to heavy rainfall by removing atmospheric instability in the gray-zone, smoothly reducing the role of CPS and increasing the role of MPS as grid spacing is decreased. Additionally, the sensitivity experiments show that the shorter CAPE timescale and decreased entrainment process resulted in fast development and exaggeration of convective activities, respectively. These parameters modulated by the scale-aware MSKF scheme can play a crucial role in the balanced effect between the CPS and MPS in the gray-zone by controlling the entrainment rate and CAPE timescale.


## Plain Language Summary

With the increasing computer resources, Numerical weather prediction (NWP) models are operating in the "gray zone" at horizontal grid spacing in the range of 1-10 km, where both cumulus parameterization and explicit resolve are problematic. This study investigates the impact of the scale-aware convective parameterization scheme (CPS) on convective cells in the simulation of heavy precipitation across the gray-zone using the Weather Research and Forecasting (WRF) model. The scale-aware CPS uses a scale-aware parameter that modulates the convective process as a function of the horizontal grid spacing. We found that simulating convection processes in the gray-zone without CPS is still limited because atmospheric instability inadequately triggers or reduces it. Moreover, the CPS without scale-awareness caused the erroneous precipitation simulation due to the exaggeration of convection and distortion of the synoptic fields. Contrastingly, the scale-aware CPS improved the simulated convection cells associated with heavy rainfall in the gray-zone by reducing the role of CPS and increasing the role of explicitly resolved precipitation as grid spacing is decreased. Results indicated that including scale-aware parameter in scale-awareness CPS plays a crucial role in controlling the CPS and MPS in the gray-zone by controlling the convective processes.

## 1 Introduction

The precipitation characteristics in Korea have altered due to a changing climate. *Ha et al.* (2005) and *Kwon et al.* (2007) showed that the East Asian summer monsoon changed since the early mid-1990s. Several studies have shown that annual rainfall in Korea has tended to increase. Notably, the frequency and intensity of precipitation increased considerably since the 1990s (*Kim et al.*, 2008; *Choi et al.*, 2013; *Mun et al.*, 2019). *Choi et al.* (2008) showed that precipitation, especially in July and August, increased significantly. *Lee et al.* (2011a) indicated that the annual precipitation amount from 2001 to 2010 considerably increased in July compared

to the past 30 years from 1970 to 2000. *Ho et al.* (2003) showed that the precipitation intensity in early August was significantly enhanced due to the spatial difference in mid-level geopotential height over the whole of Asia as a result of global warming. More than half of the annual precipitation in Korea is concentrated in the summer (*Ho&Kang*, 1988; *Park et al.*, 2008), and heavy rainfall during the summer monsoon is one of the robust characteristics of precipitation in Korea, which causes considerable socioeconomic damage (*Kang et al.*, 1992). Various precipitation systems generate heavy rainfall over the Korean Peninsula (e.g., band-type and cluster) (*Sun&Lee*, 2002; *Shin&Lee*, 2005; *Cho&Lee*, 2006). Mesoscale convective systems (MCSs) are the major types of heavy rainfall systems, which act over the Korean Peninsula during the summer monsoon. Approximately 47% of heavy rainfall events between 2000 and 2006 were associated with MCSs (*Lee&Kim*, 2007). According to the Korean Ministry of the Interior and Safety, the average annual number of death and the total property damages due to heavy precipitation from 2009 to 2018 are 11.5 people and $125 million, respectively (*MOIS*, 2019). More reliable and accurate predictions and a better understanding of the formation and development mechanisms using observation data and numerical models are necessary to reduce damage caused by heavy precipitation in Korea.

Many studies utilized a coarser horizontal grid spacing of the numerical models than the actual horizontal scale of cumulus convection due to the limitation of computing resources. At coarser resolutions with grid spacing larger than 10 km, the convective parameterization scheme (CPS) is turned on to represent the effect of subgrid-scale convection on large-scale fields by calculating the potential subgrid-scale cloud and physics of precipitation processes in association with grid-scale independent and dependent variables. With the CPS, subgrid-scale convection is possible even if the air parcel at the grid point is not saturated. Therefore, the CPS reduces delay

in precipitation or local instability, and it can represent the interaction between clouds and the surrounding environment (*Bechtold et al.*, 2014; *Freitas et al.*, 2018; *Han et al.*, 2011). Many studies (*Wang&Seaman*, 1997; *Yang et al.*, 2000) have shown that numerical simulation can be sensitive to the chosen parameterization schemes compared to those of the other factors (e.g., domain setup and studied cases). *Jankov et al.* (2007) and *Lowrey and Yang* (2008) indicated that the different parameterization schemes (e.g., CPS and microphysics parameterization scheme (MPS)) resulted in different simulation results, and especially the CPS showed a significant impact on precipitation simulation. Parameterized convection at coarse horizontal grid spacing has limitations and causes inaccurate precipitation simulations (e.g., *Emanuel&Raymond*, 1993; *Olson et al.*, 1995; *Wang&Seaman*, 1997). Therefore, efforts to improve the CPS are required to reduce the prediction error of the convection process in the subgrid-scale (*Wang et al.*, 2006; *Dudhia*, 2005).

According to tremendous numerical computing and atmospheric modeling technology that can support high-resolution modeling, the grid sizes of numerical weather models are now close to 2–10 km (*Davies et al.*, 2005; *Saito et al.*, 2006; *Charles et al.*, 2009). Although a higher resolution allows for more accurate representations of surface fields and topography, it is generally difficult to define the range of convection process between the subgrid-scale to be parameterized using CPS and the grid-scale to be explicitly resolved (*Hong&Dudhia*, 2012; *Molinari&Dudek*, 1992; *Jeworrek et al.*, 2019), which is called “gray-zone (1–10 km)” (*Gerard&oceanography*, 2007). The development of CPS for the gray-zone in the numerical model remains a problem (*Hong&Dudhia*, 2012).

Generally, the CPS is not required as explicitly resolved convections are considered sufficient in grid intervals under the gray-zone. *Wang et al.* (2015) shows that the regional

models with 9-km grid spacing can capture the salient characteristics of precipitation over the tropics without CPS. In *Molinari and Dudek* (1992) and *Weisman et al.* (1997), the horizontal grid spacing is 4 km or less, and it can explicitly consider convection-permitting without relying on CPS at this resolution. *Yu et al.* (2010) indicate that a grid size of 3 km is sufficient to resolve the convection band and CPS for this grid size is not necessary.

Contrarily, studies have shown that high-resolution numerical models only with MPS (i.e., no CPS) still have limitations in simulating convection processes (*Arakawa et al.*, 2016; *Gustafson et al.*, 2013). *Deng et al.* (2006) showed that the simulated precipitation skill of a 4-km grid improved when CPS was used. Furthermore, *Lee et al.* (2011b) showed that the numerical model improves heavy rainfall forecast by activating both the CPS and MPS at fine grid size (e.g., 3 km). There are still ambiguous results for the CPS activation at grid spacings smaller than 3 and 4 km. Consequentially, there remains an effort to adjust or improve the CPS validity in the gray-zone (*Arakawa et al.*, 2011; *Hong&Dudhia*, 2012; *Prein et al.*, 2015; *Bengtsson&Körnich*, 2016; *Zheng et al.*, 2016). Such new schemes are designed to be scale-aware, such that they can represent smooth transition grid intervals. *Sims et al.* (2017) showed that an applied scale-aware parameter, which is a function of horizontal resolution, determined the simulation performance of mesoscale convection phenomena, and the Kain-Fritsch scheme (KF) modified by the scale-aware parameter could improve the convection timing of the mesoscale convection phenomenon in the Carolinas region. *Kwon and Hong* (2017) applied the scale-aware parameters in the Simplified Arakawa-Schubert scheme at 3 km, which improved simulated precipitation over the Korean Peninsula by the summer monsoon. A study by *Jeworrek et al.* (2019) consisted of five domains with different horizontal model resolutions (27, 9, 3, 1, and 0.3 km) to investigate the predictability of the CPSs with scale-aware parameters in the gray-

zone. Their study testing the effect of scale-aware CPS showed significant improvement in the location, pattern, and intensity of precipitation at high resolution. The role of CPS is gradually reduced to reproduce the smooth reduction from subgrid-scale to grid-scale precipitation with increasing resolution.

Summarily, the physics of the sub-grid precipitation process plays an essential role in the simulation of precipitation over the Korean Peninsula, and studies showed that the importance of smooth CPS activation using scale-aware parameters increased with higher resolution (*Alapaty et al.*, 2012; *Sims et al.*, 2017; *Kwon&Hong*, 2017; *Jeworrek et al.*, 2019). Thus far, various numerical studies have been conducted to understand the effect of high-resolution models in simulating heavy rainfall events over the Korean Peninsula (*Hong&Lee*, 2009; *Kwon&Hong*, 2017). However, studies on the role of scale-aware parameterization schemes in the gray-zone are still limited for heavy rainfall cases in the Korean Peninsula. Therefore, this study investigated the effect of scale-aware parameters on a gray-zone domain using non-scale-aware and scale-aware CPS for a heavy rainfall case in Korea. In this study, the KF (*Kain*, 2004) and the Multi-scale Kain-Fritsch (MSKF) schemes (*Zheng et al.*, 2016) are selected for CPSs. The MSKF scheme is a scale-aware version of the KF scheme, in which the CAPE timescale and entrainment rate are adjusted according to the horizontal grid spacing. A flash flooding event in the central region of the Korean Peninsula from 15 to 17 July 2017, is selected as the heavy rainfall case. The case is spatially and temporally localized and is suitable for analyzing precipitation sensitivity to the applied non-scale and scale-aware CPS in the gray-zone.

Simulations of numerical models are influenced by various CPS factors, such as the CAPE timescale and entrainment rate. In the model, the CAPE timescale plays a role in the dissipation of the deep moist convection instability during that period and determines the cloud

lifetime (*Mishra&Srinivasan*, 2010). Additionally, the entrainment rate changes the convective process by determining the saturation and mixing with the surrounding dry air (*Lin&Arakawa*, 1997; *Kuang&Bretherton*, 2006; *Khairoutdinov&Randall*, 2006). Therefore, we conducted sensitivity experiments to examine the impacts of the scale-aware parameter on the CAPE timescale and entrainment rate in the MSKF scheme.

The rest of the paper is organized as follows. Section 2 describes the studied heavy rainfall case and numerical experimental design. Section 3 shows the results from the numerical experiments with different CPSs and sensitivities to the scale-aware parameter. Finally, the summary and conclusions are provided in Section 4.

## 2 Case and Experimental Design

### 2.1 Characteristics of Cheong-ju rainfall case

A significant amount of extreme precipitation was recorded in Cheong-ju city on 16 July 2017 (Figure 1a), with a maximum daily rainfall of 290.2 mm. In Choeng-ju (marked as a red star in Figure 1a), the rainfall started at 2000 UTC, 15 July (0500 LST, 16 July), and the first and second peaks occurred at 2300 UTC, 15 July and 0200 UTC, 16 July, respectively (Figure 1b). Hourly rainfall rates peaked at 2300 UTC with 86.2 mm $hr^{-1}$ and 0200 UTC with 67.5 mm $hr^{-1}$. Subsequently, the rainfall almost stopped at 0300 UTC on 16 July 2017.

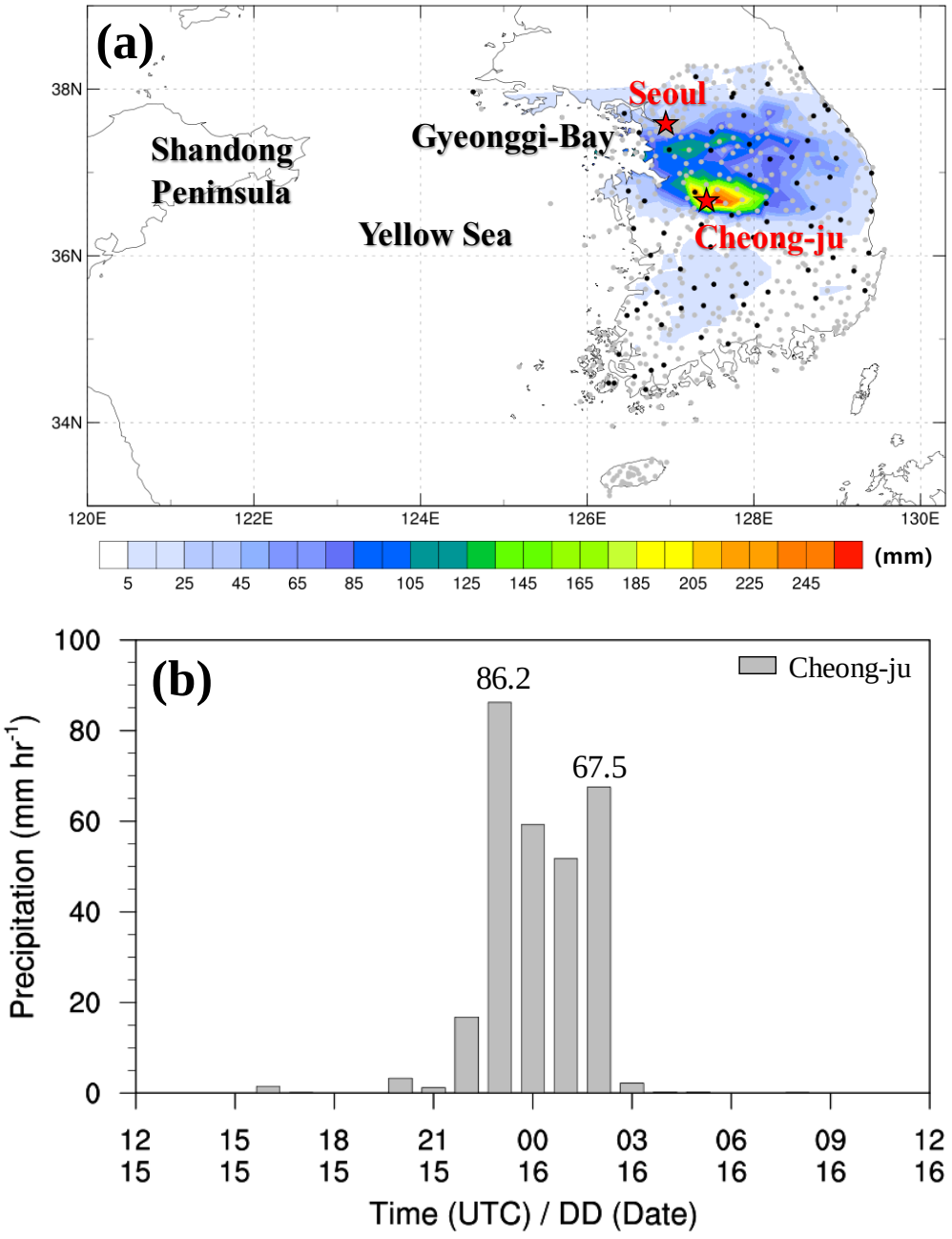


**Figure. 1**. (a) Map of the study area showing the 24-hour accumulated rainfall amounts (mm) observed by automated surface observation systems (ASOS, black dots) and automatic weather stations (AWS, gray dots) in the central Korean Peninsula from 1200 UTC (2100 LST), 15 to 1200 UTC (2100 LST), 16 July 2017 (The star mark denotes the location of Seoul and Cheong-ju), and (b) Bar plot of the time series of hourly rainfall from 1200 UTC (2100 LST), 15 to 1200 UTC (2100 LST), 16 July 2017.

Figure 2 shows the synoptic fields of four pressure levels analyzed by the FNL 0.25° reanalysis data at 1800 UTC, 15 July 2017, which was 6 h before the maximum precipitation intensity in Cheong-ju. At 200 hPa (Figure 2a), an upper-pressure trough developed west of the Shandong Peninsula and a shallow upper-pressure ridge in the south of the Shandong Peninsula extending to South Korea. Figure 2b and d show that the western North Pacific subtropical high (WNPSH) is expanded to the Korean Peninsula, forming a confluent flow region, and warm and humid water vapor is transported into the central region in the Korean Peninsula. Notably, positive relative vorticity is dominant over the central region of the Korean Peninsula, where the southwesterly enhances continuous moisture transportation (Figure 2b). Additionally, the divergence areas are consistent with the water vapor convergent flow areas at the lower level (i.e., the Shandong Peninsula and the Korean Peninsula), indicating that both dynamic and thermodynamic environments induced rising motion at the mid-level (see supplementary Figure S1). Due to the unstable conditions, the quasi-stationary front (Changma front) is initiated from the west of the Shandong Peninsula (along the isotherm of 333 K in Figure 2c), where a robust upper-level trough expands to the Korean Peninsula. Environmental conditions such as upper-level divergence, abundant water vapor supply, and significant atmospheric instability are favorable for developing a convection system. *Chung et al.* (2019) found that warming in the northern part of the Changma front resulted in less meridional temperature contrast and an unstable atmosphere repeating a small disturbance that has moved along the boundary in the WNPSH, which resulted in discontinuous cloud bands and intermittent rainfall. A discontinuous broken Changma front with strong convective cells is represented through the 3-hourly enhanced IR satellite images from 1600 UTC, 15 July to 0100 UTC, 16 July (Figure 3). In the enhanced IR images, there are two convective cells: a convective cell (hereafter referred to as CC1) that has

begun to develop off the coast of Gyeonggi-bay and a deep-developed convective cell (hereafter called CC2) in the south of Shandong Peninsula. Eventually, the CC1 generated on Gyeonggi-bay gradually developed and advanced to the southeast (Figure 3a and b). All precipitation of this investigated event was associated with CC1. Another convective cell (i.e., CC2) developed in the south of the Shandong Peninsula, which moved into the Yellow Sea over time. These cloud systems result from the rising motion and substantial low-level convergent area from the activated quasi-stationary front accompanied by heavy rainfall.

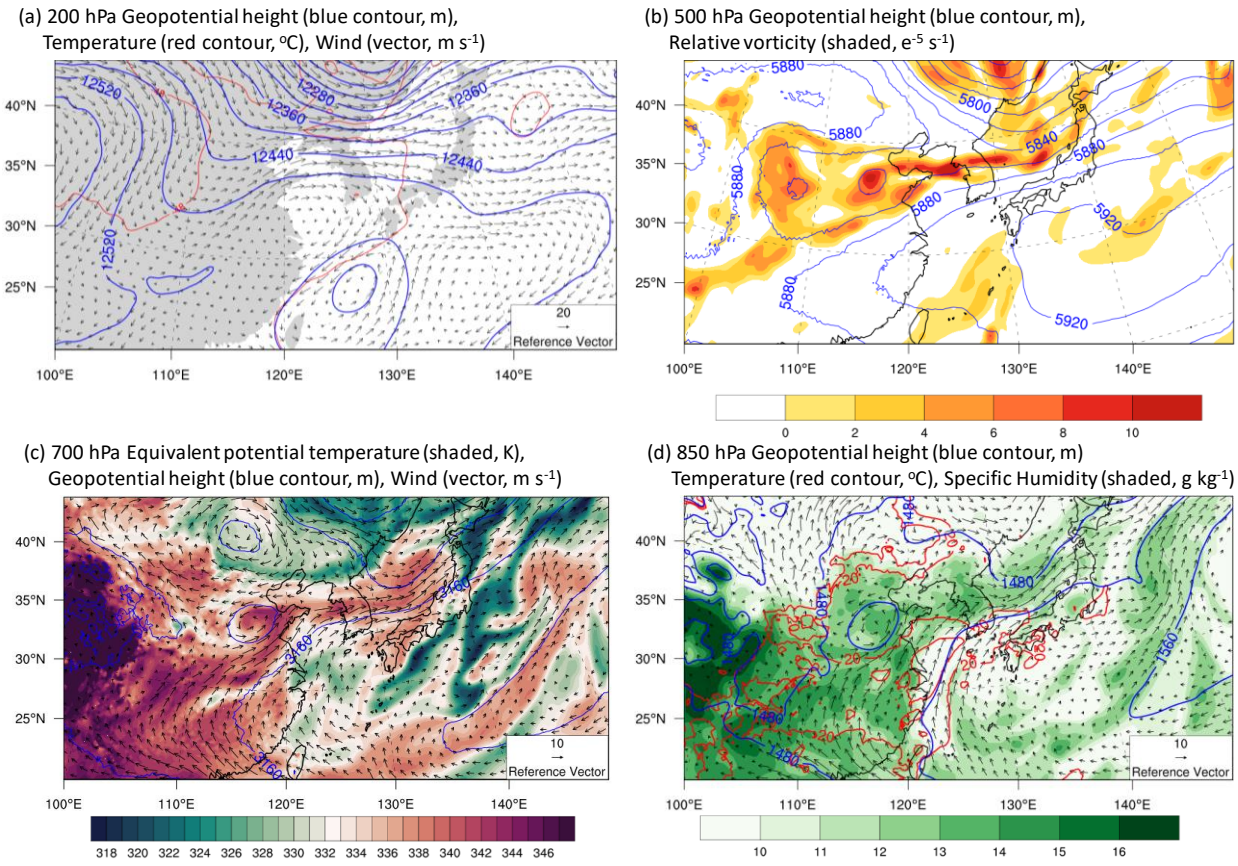


**Figure. 2**. Spatial contour maps showing the synoptic fields from FNL 0.25° reanalysis data at 1800 UTC, 15 July 2017.

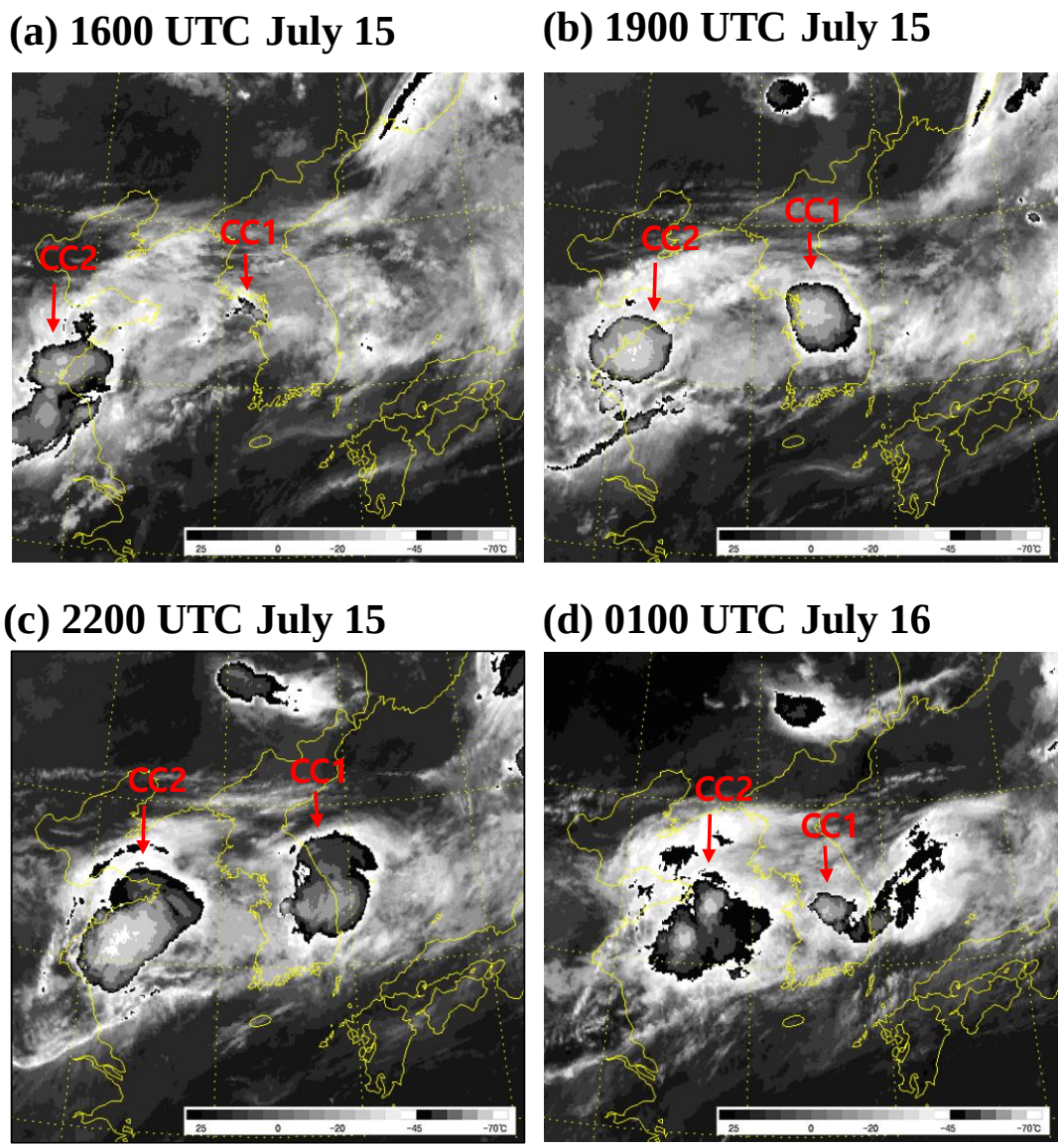


**Figure. 3**. Three-hourly Enhanced IR satellite images showing cloud system development between 1600 UTC, 15 July and 0100 UTC, 16 July 2017.

## 2.2 Model configuration and experiment design

The Advanced Research WRF model (Skamarock et al., 2008) Version 4.1 was used in this study, and the initial and boundary conditions were obtained from the 1° × 1° reanalysis data

238 of the National Centers for Environmental Prediction/National Centers for Atmospheric
239 Research (NCEP/NCAR) Final analysis (FNL). The model consisted of four domains with 36 km
240 (201×201), 12 km (352×352), 4 km (460×460), and 1.33 km (201×201) horizontal grid spacings,
241 which included CPS gray-zone resolution (Figure 4a). We used two-way nested domains with a
242 Lambert conformal map projection. The domain contained 32 vertical levels from the surface to
243 the top of the atmosphere at 50 hPa. The model used the WSM6 cloud microphysics scheme
244 (*Hong&Lim*, 2006), the Yonsei University planetary boundary layer scheme (*Noh et al.*, 2003;
245 *Hong et al.*, 2006), Dudhia short-wave radiation scheme (*Dudhia*, 1989), and long-wave
246 radiation scheme based on the rapid radiative transfer model (*Mlawer et al.*, 1997). In this study,
247 the KF scheme and MSKF schemes were selected for the sensitivity experiments. The KF
248 scheme is a sub-grid scheme with deep and shallow convection and uses a mass flux approach to
249 calculate the CAPE-based closure assumption scheme. The MSKF scheme is a scale-aware
250 version of the KF scheme. Compared to the KF, the MSKF includes changes in the convective
251 adjustment timescale and improvements to the entrainment formulations (*Zheng et al.*, 2016).
252 The MSKF also incorporates a grid-aware scaling parameter into these modifications. The main
253 advantages of the MSKF scheme are as follows.
254

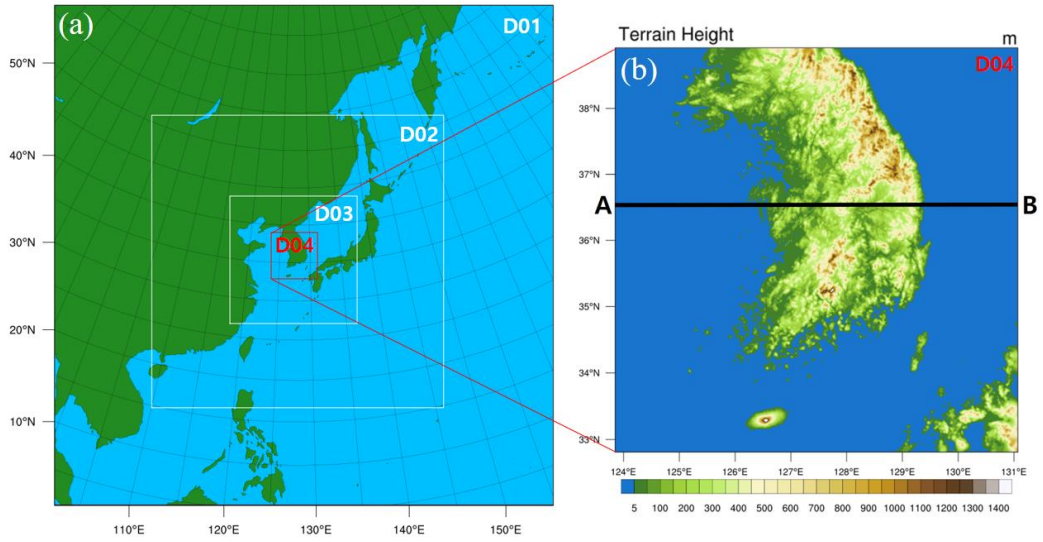


**Figure. 4.** Map showing (a) Four nested domains with 36 km, 12 km, 4 km, and 1.33 km grid spacing in WRF, and (b) terrain height for the finest domain (red box identified as the D04 domain in Figure 4a). Line AB in Figure 4b marks the vertical cross-section used in Figure 10.

Both the KF and MSKF schemes remove 90% of the potential energy within the CAPE timescale period (*Bechtold et al.*, 2001), and the CAPE timescale is limited to 1800 s and 3600 s in the cloud layer for deep and shallow convections, respectively. The convection time step ($\tau$) connected to the CAPE timescale of clouds is proportional to the grid length *DX* (*Fritsch et al.*, 1976; *Fritsch&Chappell*, 1980). The CAPE timescale works to effectively resolve atmospheric instability at coarse grid resolution. However, the higher model grid resolution leads to an increase in the unresolved cloud area and faster saturation speed, which causes rapid CAPE removal problems within the CAPE timescale resulting in intense precipitation. For reduction of these inadequacies, the MSKF scheme uses the adjustment timescale $\tau$ (s) based on *Bechtold et al.* (2008), which is multiplied by the scaling parameter ($\beta$) impacted by the horizontal grid-scale (*Zheng et al.*, 2016).

The CAPE adjustment timescale can be estimated as:

$$\tau = \frac{H}{(\delta m_b A_e)^{\frac{1}{3}}}\beta, \quad (1)$$

where $H$ is cloud depth (m), $\delta m_b$ is the updraft mass flux of cloud base per unit density (m $s^{-1}$), $A_e$ is the potential energy of the saturated air supplied to the cloud base ($m^2$ $s^{-2}$), and $\beta$ is the scaling parameter defined as

$$\beta = 1 + \ln\left(\frac{25}{DX}\right). \quad (2)$$

β is set to approximately 2.8 and 4.2 at 4 and 1 km model grid spacings in equation (2), respectively. As the grid spacing decreases, the CAPE adjustment timescale using the scale-aware parameter becomes longer. A longer CAPE timescale allows slower elimination convective instability.

Additionally, the MSKF scheme adjusts the minimum entrainment rate using the scale-aware parameter similar to the timescale concept. The adjusted entrainment rate is defined as:

$$\Delta M_e = M_b \frac{\alpha\beta}{z_{LCL}}\Delta p, \quad (3)$$

where $M_b$ is the updraft mass flux per unit area (kg $s^{-1}$) at the cloud base, $\beta$ is the scale-aware parameter (eq. 2), $\Delta p$ is the pressure depth of a model level (Pa), and $Z_{LCL}$ (m) is the height of the cloud base. The value of $\alpha$ (0.03) is a constant parameter (*Tokioka et al.*, 1988). The cloud base height replaces the arbitrarily fixed cloud radius because entrainment is associated with the sub-cloud layer depth. The mixing rate increases with the β value, limiting the sub-grid convection (*Lin et al.*, 2013). This adjusted scale-aware entrainment formulation allows the mixing rate, $\Delta M_e$, to increase with decreasing horizontal grid spacing. At higher resolutions, the effects of the KF scheme are reduced, which inhibits deep convection.

293 The experiments conducted in this study consist of two parts. In Part 1, three experiments
294 were conducted to investigate the difference between the KF and MSKF schemes and the impact
295 of CPS in the gray-zone (KF_D12, KF, and MSKF runs). The KF_D12 run employed the KF
296 scheme only in D01 and D02 domains with 36 and 12 km resolutions, respectively, while the KF
297 and MSKF runs used the KF and MSKF schemes in all domains, respectively. In Part 2, we
298 conducted two additional experiments (CTS and ENT) to investigate the effects of the scale-
299 aware parameter in the MSKF scheme on the convective activity simulation causing heavy
300 rainfall. The CTS run is the same as the MSKF run but for the scale-aware parameter value of 1
301 in the CAPE timescale (i.e., the same CAPE timescale as in the KF scheme), and the ENT run is
302 identical to the MSKF scheme except for the same entrainment rate as in the KF scheme. As the
303 horizontal model resolution increases (e.g., D03 or D04 domains), we can examine the effect of
304 the scale-aware parameter on the reduced (increased) CAPE timescale (entrainment rate) of the
305 MSKF scheme by comparing the CTS (ENT) and MSKF runs. The experiments conducted in
306 this study are summarized in Table 1.

307 Table 1. List of experiments conducted in this study.

| Experiments | Description |
|---|---|
| KF_D12 | KF scheme used only for the D01 and D02 domains |
| KF | KF scheme used for all domains |
| MSKF | MSKF scheme used for all domains |
| CTS | Same as MSKF run, but for the same CAPE timescale as in KF scheme |
| ENT | Same as MSKF run, but for the same entrainment as in KF scheme |

308

# 3 Results

## 3.1 Difference between the KF and MSKF schemes and CPS impact on the gray-zone

In this section, simulated precipitation from the KF_D12, KF, and MSKF runs was compared with the Integrated Multi-SatellitE Retrievals for Global Precipitation Measurement (IMERG, *Huffman et al.*, 2015a; 2015b) and FNL 0.25° reanalysis data to analyze the differences in rainfall and synoptic fields among the three runs. As mentioned in Figure 3, two types of precipitation zones were observed in Figure 5a. One was the precipitation zone caused by CC1, which started over the Seoul metropolitan region (Gyeonggi-bay) and moved southeastward. Another related to CC2 moved from the Shandong Peninsula to the Yellow Sea. The IMERG satellite image indicates that the precipitation area related to CC1 over Gyeonggi-bay moved southeastward, resulting in heavy rainfalls in Cheong-ju. Figure 5b-d shows the 3-hourly accumulated total (subgrid-scale and grid-scale) precipitation in the D02 domain of three runs. In the KF_D12 run (Figure 5b), CC1 was located over the eastern part of Seoul and was expanded northeastward; the model simulated simply one convective system instead of two convective systems. Furthermore, unreasonable shifting of the simulated precipitation associated with CC2 to the Yellow Sea instead of the southern part of the Shandong Peninsula caused an error of overestimated rainfall in the ocean. The KF run (Figure 5c) simulated similar features to the KF_D12 run (i.e., overestimated precipitation over the Gyeonggi-Bay). However, the precipitation core was shifted west in KF run compared to the KF_D12 run. Contrastingly, the MSKF run (Figure 5d) reproduced the spatial pattern of simulated precipitation more correctly relative to KF_D12 and KF runs. Notably, in the MSKF run, CC1 and CC2 were simulated separately, similar to those in the IMERG. Hence, the heavy rainfall related to CC1 was reasonably captured.

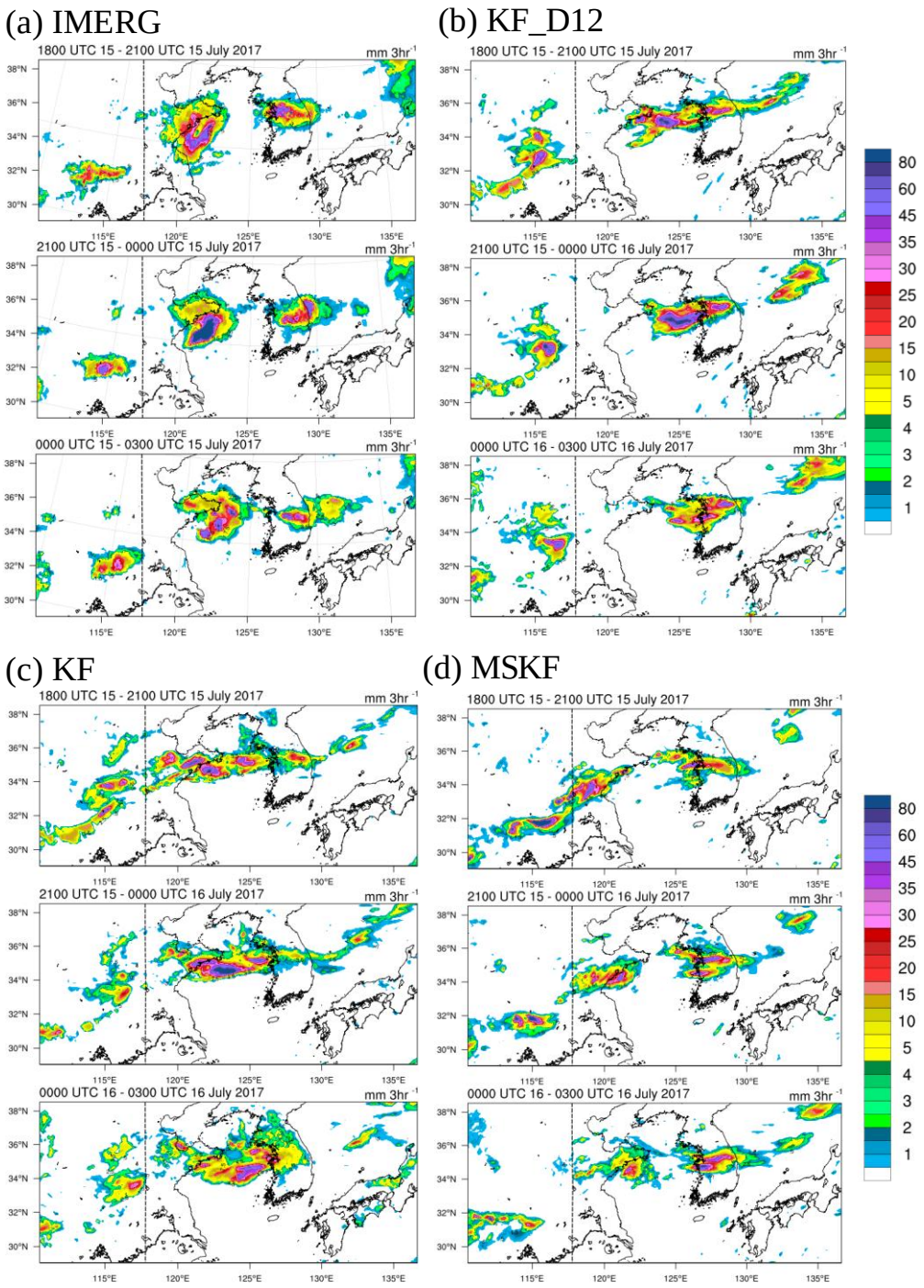


**Figure.** 5. Spatiotemporal images showing three-hourly accumulated total precipitation (mm) in the D02 domain between 1800 UTC, 15 July and 0300 UTC, 16 July 2017. Black dashed lines indicate the left boundary of the D03 domain in Figure 3a.

Figure 6 shows the time series of domain-averaged hourly precipitation for observed (IMERG) and simulated precipitation (i.e., the D02 domain) averaged for the target region, including the Korean Peninsula and the Yellow Sea. Heavy precipitation was observed for 18 hours (1200 UTC, 15 July to 0300 UTC, 16 July), with two peaks at 1800 UTC 15 and 0300 UTC 16. However, the KF_D12 run reproduced the two heavy precipitation peaks earlier than in the observation with the overestimated precipitation due to unreasonable simulation in the Yellow Sea. The simulated precipitation of the KF run is more reasonable than the KF_D12 run. However, the precipitation in the target region was still overestimated than IMERG. Contrastingly, the MSKF run simulated heavy precipitation most reasonably in the target region in terms of amount.

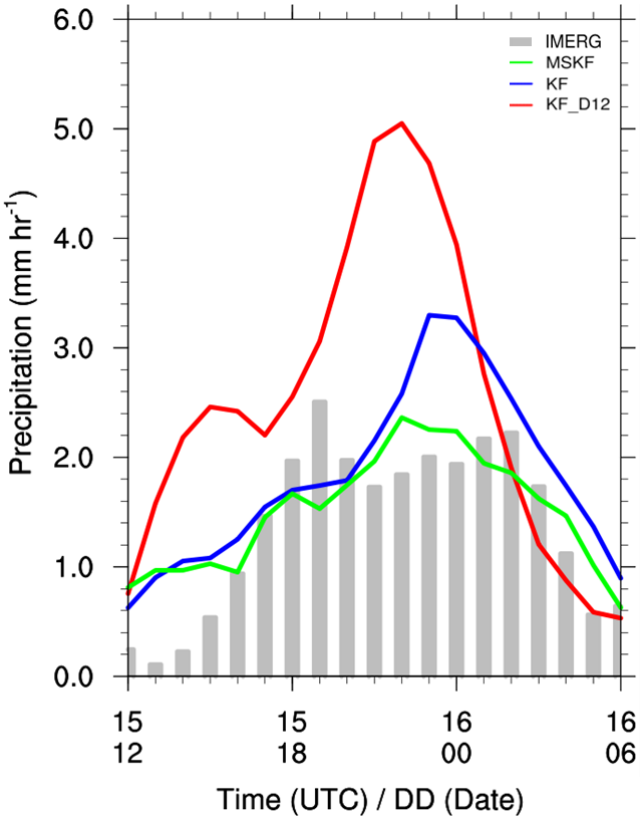


**Figure. 6**. Graph depicting time-series of hourly accumulated rainfall averaged between 36-38 °N and 123-130 °E for the IMERG (gray box), KF_D12 (red line), KF (blue line), and MSKF

(green line) run. Simulated precipitation is calculated from the results of the 4-km resolution domain.

To quantitatively evaluate the performance of the heavy precipitation simulation (Figure 7), we calculated two standard skill scores (i.e., the treat score (TS) and bias score (BS)) for precipitation with various precipitation intensity thresholds (e.g., 0.5, 5, 10, 20, 30, 40, and 50 mm). Two scores were calculated using the following equations (Eq. 4 and 5) (Wilks, 2011). As BS and TS approach 1, the accuracy of the model in forecasting rainfall events increases.

$$\mathrm{BS} = \frac{Hits+False\ alarms}{Hits+Misses}, and \quad (4)$$

$$\mathrm{TS} = \frac{Hits}{Hits+False\ alarms+Misses}. \quad (5)$$

The precipitation detection skills (e.g., BS and TS) decreased as the threshold increased in the three runs (Figure 7). The TS for the precipitation forecast is the highest in the MSKF run compared to the other runs (e.g., the KF_D12 and KF runs) for all the considered precipitation thresholds. In the TS, the KF and KF_D12 runs have a low score than the MSKF run across the entire range of precipitation intensity thresholds. The result of the BS indicates that the KF and KF_D12 runs simulated more ‘false alarms’ and ‘misses’ than ‘hits’ compared to those of the MSKF run. In the BS, the MSKF run has high model performance in detecting precipitation across the entire range of precipitation intensities by maintaining the BS value of around 1. However, the BS in the KF and KF_D12 runs increases more significantly than in the MSKF run. Notably, the BS in the KF_D12 run increases dramatically as the threshold increases, suggesting that in the low performance of the KF_D12 run, the number of falsely classified grid

373 boxes as ‘false alarms’ tends to be substantially larger than the number of incorrectly classified
374 grid boxes as ‘misses’. The KF_D12 run has many ‘false alarms’ due to excessive precipitation
375 in the Yellow Sea before entering the Koran Peninsula. In the KF and KF_D12 runs, as a result,
376 the overall forecasting abilities of the precipitation products in capturing the correct magnitude
377 of intense precipitation are less accurate than that in the MSKF run.

378

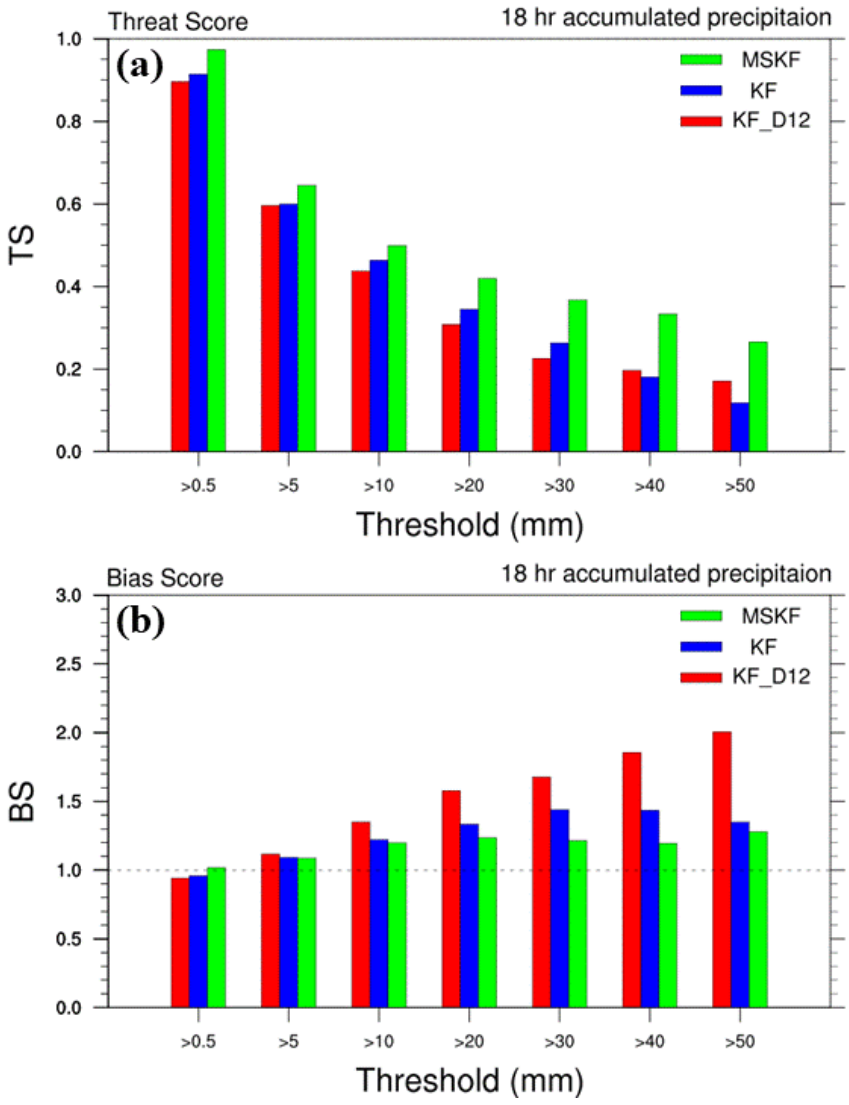


379
380

381 **Figure. 7**. Bar plots of the statistical indices corresponding to the KF_D12, KF, and MSKF runs
382 with IMERG based on different thresholds of 18-hourly accumulated precipitation (from 1200

383 UTC, 15 July to 0600 UTC, 16 July 2017). The simulated precipitation is interpolated to the
384 observation grid points, and model statistics are calculated for South Korea and the Yellow Sea
385 (between 36-38 °N and 123-130 °E).
386
387 Figure 8 shows the distribution of subgrid-scale precipitation simulated by the CPS. The
388 KF run simulated subgrid-scale precipitation is similar to the KF_D12 run in the D02 domain
389 outside the D03 domain. However, within the D03 domain, only the KF run simulated subgrid-
390 scale precipitation employing CPS for the domain. The KF_D12 run could not produce subgrid-
391 scale precipitation because of the absence of CPS in the D03 domain. Contrastingly, the subgrid-
392 scale precipitation simulated in both the D02 and D03 domains of the MSKF run was reduced
393 compared with that in the KF run. The MSKF scheme simulates a smaller ratio of subgrid-scale
394 precipitation to total precipitation than in the KF scheme as the horizontal resolution increases
395 because the scale-aware parameter in the MSKF scheme smoothly decreases the role of CPS and
396 increases the removal of atmospheric instability by MPS.

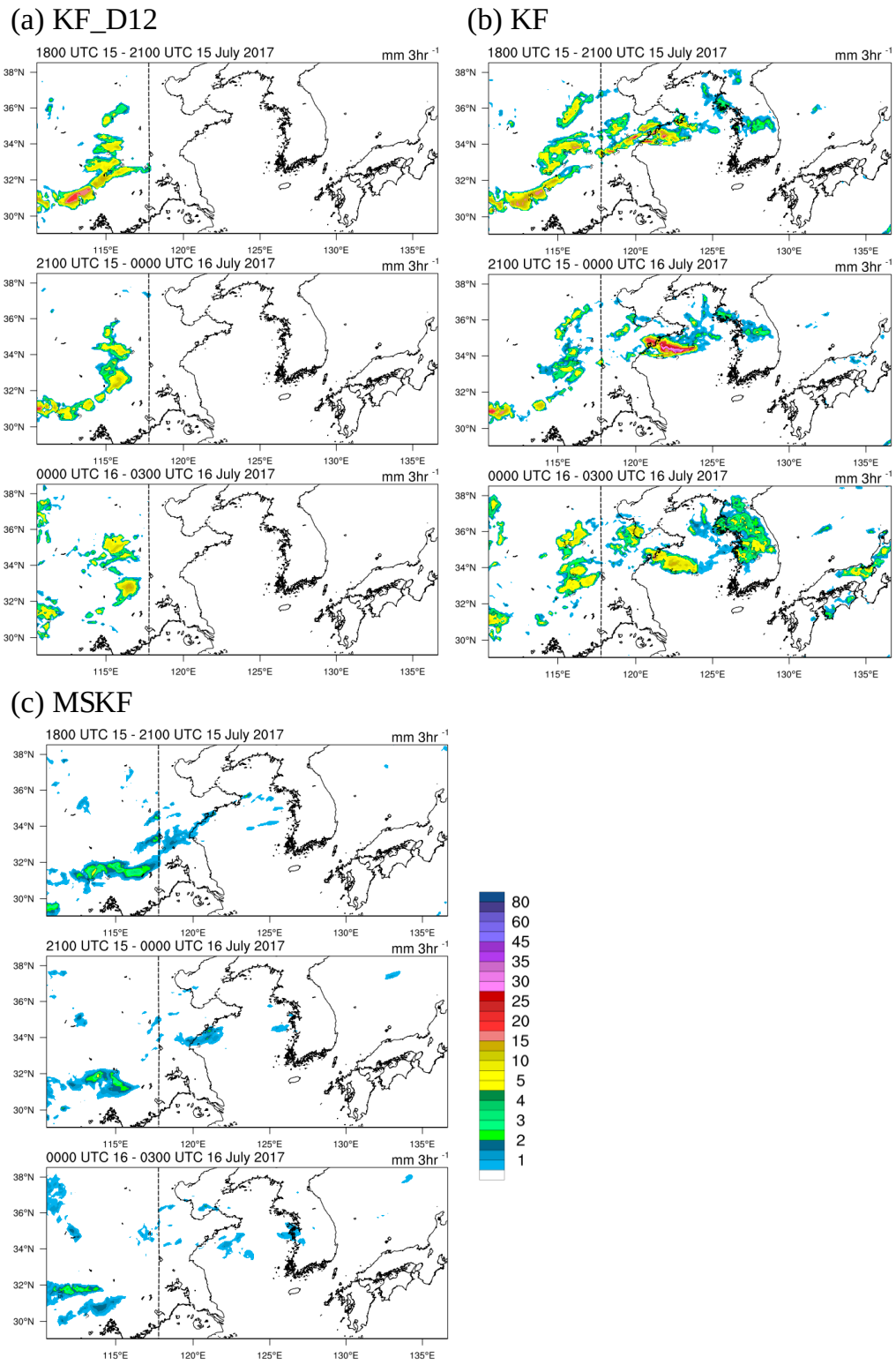


**Figure. 8**. Spatiotemporal images (similar to Figure 5) for three-hourly accumulated subgrid-scale precipitation (mm).

To investigate the causes of the different simulations among the three runs, we analyzed the synoptic conditions from the reanalysis and simulations of the D02 domain in Figure 9. In FNL (Figure 9a), LLJ (> 13 m $s^{-1}$) transporting wet and warm air was located in two regions (e.g., the Shangdong and Korean Peninsulas) with heavy precipitation. (see Figure 5a). The three WRF runs reproduced wet and warm air transport by LLJ from inland China to the Korean Peninsula. However, the LLJ cores were inappropriately located in inland China and the Yellow Sea in the KF_D12 and KF runs (Figure 9b, c), and the intensity of LLJ was overestimated, which induced enhanced moisture transport. Notably, LLJs located at the Shandong Peninsula in the reanalysis were further shifted to the Yellow Sea in the KF_D12 run. Additionally, low-pressure systems at 700 hPa unrealistically developed in the LLJ cores in the KF_D12 and KF runs. More moisture transported by the enhanced LLJ led to increased convective instability over the regions, which developed convective activities and low-level pressure erroneously. Contrarily, the MSKF run reproduced the low-pressure system and LLJ similar to the reanalysis regarding location and intensity.

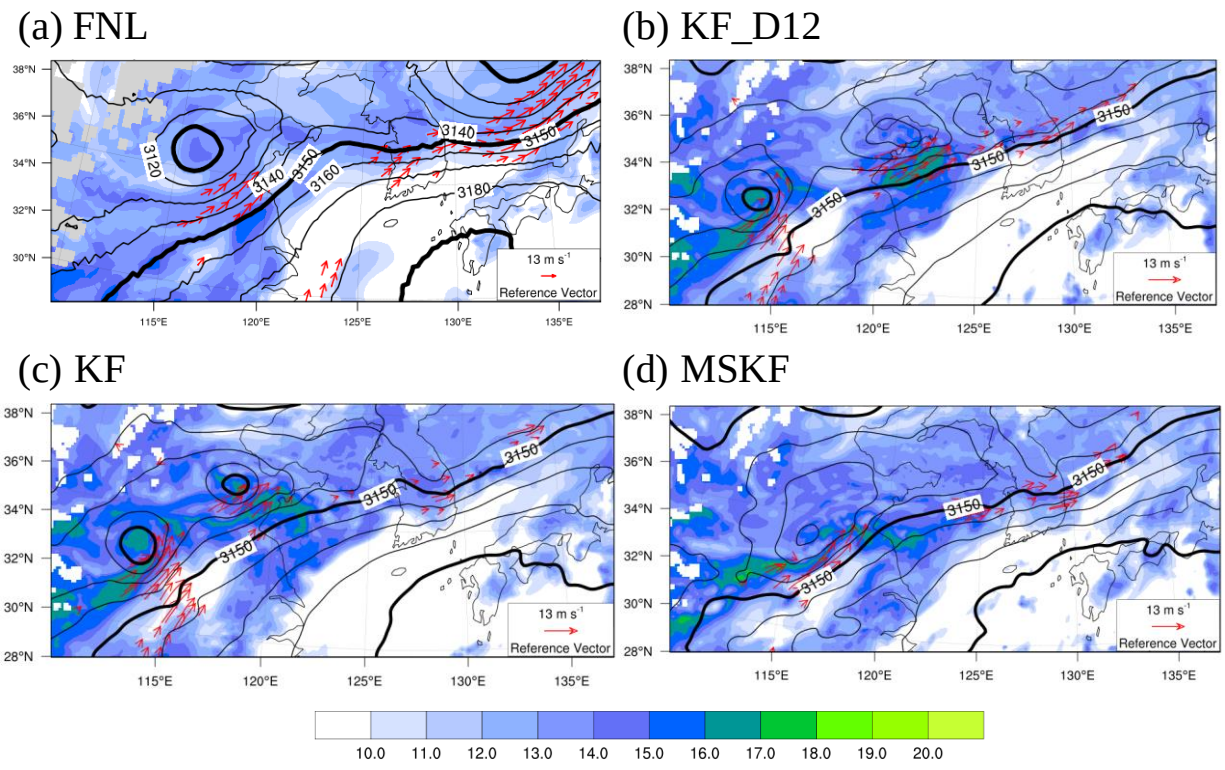


**Figure. 9**. Spatial contour maps of the wind (>13 m $s^{-1}$, red vector) and water vapor (g $kg^{-1}$, shaded) at 850 hPa, and geopotential height (m, black lines) at 700 hPa in the D02 domain at 1800 UTC, 15 and 0000 UTC, 16 July 2017.

The locations of LLJ cores were consistent with those of the heavy precipitation area in the three runs, implying that LLJ played a significant role in the development of heavy precipitation by transporting wet and warm air from the subtropics. While the KF_D12 run only eliminated atmospheric instability by MPS in the D03 and D04 domains, the MPS could not adequately trigger convection over the Shandong Peninsula. The MPS unreasonably removed the atmospheric instability in the Yellow Sea rather than the peninsula. Additionally, the MPS prominently overestimated convection in the Yellow Sea, further increasing heavy precipitation in the region by enhancing LLJ and moisture convergence. Contrarily, subgrid-scale precipitation in the Shandong Peninsula in the KF run implied that convection was developed in

434 the proper location. However, the action of CPS was excessive, which led to the distortion of
435 synoptic fields such as intensified LLJs and increased moisture convergence in the Shandong
436 Peninsula and the Yellow Sea. Thereby, MPS also simulated considerable grid-scale
437 precipitation in the regions, indicating unreasonable overestimation of total precipitation by CPS
438 and MPS. However, in the MSKF run, subgrid-scale precipitation was decreased due to
439 decreasing role of CPS compared with that in the KF run. Therefore, similar to the IMERG, the
440 MSKF run reasonably captured torrential rainfall over the Shandong Peninsula associated with
441 CC2 and heavy precipitation in the Korean Peninsula related to CC1.

442 These results imply that high-resolution simulation of convective activities by MPS alone
443 could lead to inappropriate overestimation of precipitation, as atmospheric instability may not be
444 adequately reduced. Furthermore, CPS without scale-awareness may lead to the erroneous
445 simulation of heavy precipitation at high resolution due to the exaggeration of convection and
446 distortion of the synoptic fields. Therefore, the simulation of heavy precipitation using a high-
447 resolution model would require a scale-aware CPS.

448 3.2. Sensitivity run results for rainfall and synoptic environment

449 The previous section showed that the MSKF run improved the heavy precipitation
450 simulation in the Cheong-ju region compared to the KF_D12 and KF runs; because the MSKF
451 scheme represents an incorporative transition from the CPS-induced precipitation to MPS-
452 induced precipitation in the gray-zone. To investigate the reason for the improved simulation of
453 heavy precipitation in the MSKF run, we conducted two additional sensitivity experiments on the
454 scale-aware parameter of the MSKF scheme: (1) the CTS run, which modified the CAPE
455 timescale, and (2) the ENT run, which changed the entrainment rate.

Figure 10 shows the simulated total precipitation, subgrid-scale precipitation, and synoptic fields reproduced by CTS and ENT runs. In Figure 10a, the CTS run captured the heavy precipitation zones related to CC1 and CC2, similar to the MSKF run (see top panel of Figure 5d). However, the simulated precipitation zone in the Yellow Sea caused by CC1 was further shifted westward, and subgrid-scale precipitation was simulated marginally more in the Yellow Sea than in the MSKF run (Figure 10b), suggesting that the reduced CAPE timescale of the CTS run compared to that of the MSKF run led to the faster removal of the atmospheric instability. The reduced CAPE timescale of the CTS run resulted in the rapid development of convective activities in the Yellow Sea rather than the Korean Peninsula (Figure 10b), which unreasonably enhanced moisture convergence and LLJ at 850 hPa (Figure 10c). Thus, the CTS run simulated grid-scale precipitation in the Yellow Sea earlier than in the MSKF run and corresponding observation due to the distorted synoptic conditions. Contrastingly, the ENT run (Figure 10d) unrealistically simulated the merged precipitation zone in the Yellow Sea, which is similar to the KF run (Figure 5c). Compared to the CTS and MSKF runs, the ENT run tends to overestimate subgrid-scale precipitation in the Yellow Sea because the entrainment rate was relatively weak due to the absence of scale-aware parameters (Figure 10e). Therefore, the ENT run simulated enhanced convective activities and excessive sub-grid precipitation in the Yellow Sea by CPS. Furthermore, the enhanced convective activities led to the distortion of synoptic fields, such as intensified LLJ and the exaggerated moisture convergence, which caused excessive grid-scale precipitation in the Yellow Sea (Figure 10f). Therefore, the MSKF scheme could improve heavy precipitation because of increasing CAPE timescale and enhanced entrainment process, which led to modulating atmospheric instability. In other words, the subgrid-scale (grid-scale) precipitation by the CPS (MPS) smoothly decreased (increase) in the MSKF run as the horizontal

resolution increased within the gray zone. The ENT run had a more significant error in simulated precipitation than in the CTS run, indicating that the enhanced entrainment rate of the MSKF scheme contributed more than the increased CAPE timescale to the improved simulation of heavy precipitation.

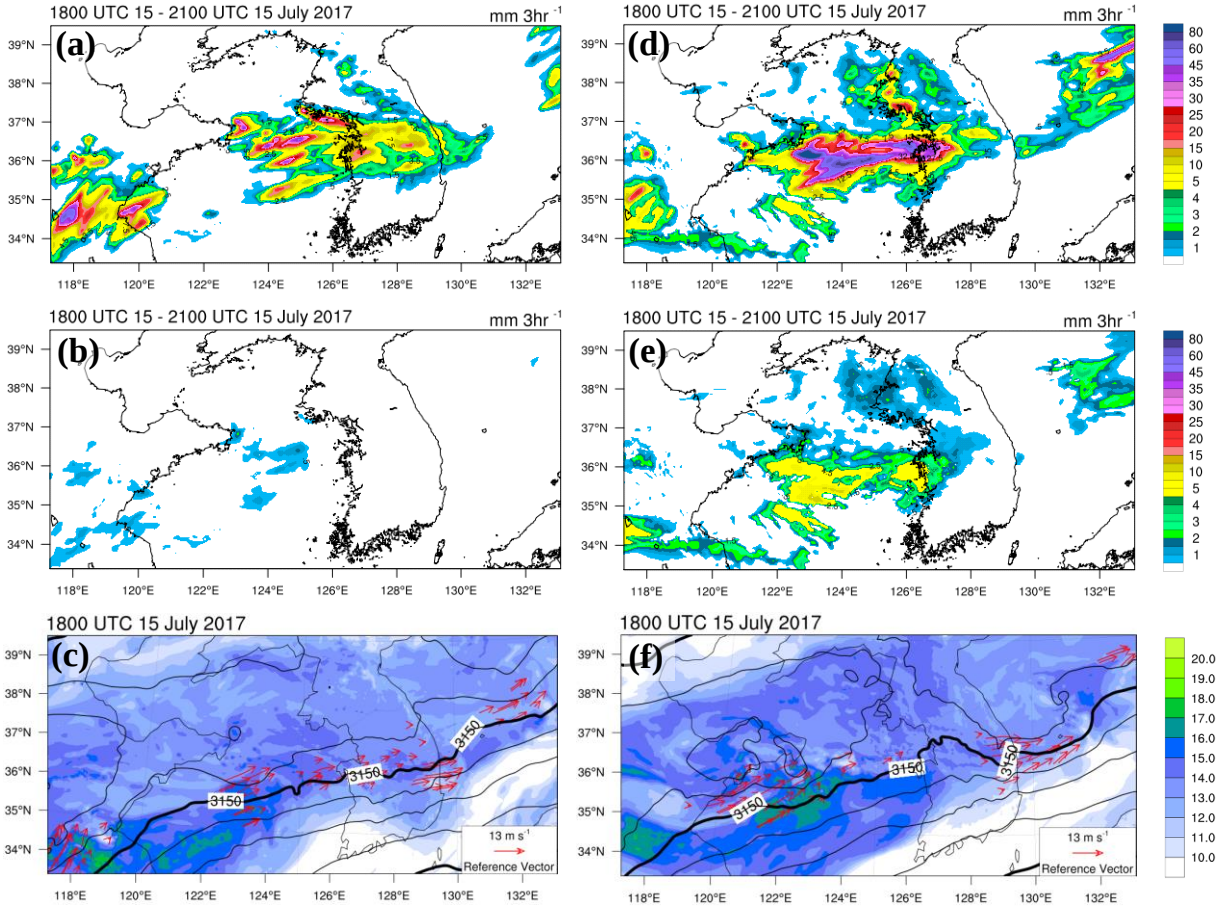


**Figure. 10**. Spatiotemporal maps of the (a, d) total precipitation (mm) and (b, e) convective precipitation (mm) between 1800 and 2100 UTC, 15 July 2017 (c, f) 850 hPa wind (m $s^{-1}$, red vector) and water vapor (g $kg^{-1}$, shaded), and 700 hPa geopotential height (m, black lines) at 1800 UTC, 15 July 2017, in the D03 domains of the CTS (left panels) and the ENT runs (right panels).

To investigate the effect of scale-aware parameters on convective development, in Figure 11, we examined the vertical fields across the region where the difference in precipitation was prominent between the sensitivity runs (see solid line in Figure 4b). The D04 domain results were used to analyze the small-scale features, and the analysis time was 2100 UTC on 15 July , which was an appropriate time to examine the effects of the scale-aware parameter. Figure 11 shows a notable difference in the vertical distribution of the equivalent potential temperature (EPT) as compared to those of the other experiments from the Yellow Sea (123.6 °E) to the Cheong-ju region (127.9 °E). The CTS run simulated high EPT at the low-level in the Yellow Sea, which increased atmospheric instability and then unreasonably developed intense convective activities between 124.5 - 125.5 °E (Figure 11a). As shown in Figure 10b, the shorter CAPE timescale in the CTS run than in the MSKF run triggered convection earlier in the Yellow Sea rather than in the west coast of the Korean Peninsula. The earlier developed convection in the Yellow Sea enhanced LLJ and moisture convergence, resulting in an increase in atmospheric hydrometeors, which could cause excessive grid-scale precipitation (Figure 11d). Also, convection was not prominently simulated in the inland of the Korean Peninsula, and relatively fewer hydrometeors were resolved. Hence, torrential precipitation in Cheong-ju was not sensibly captured (see Figure 10a). Similarly, the ENT run also simulated high EPT at the low-level. The entrainment process, which mixed moist and warm air within convective clouds with dry and cold environment air, was not strengthened because of the absence of a scale-aware parameter (Figure 11b). High EPT led to an unstable atmosphere and overestimated convective precipitation in the Yellow Sea, as shown in Figure 10b. The distorted LLJ and water vapor convergence, resulting in increased atmospheric hydrometeors and then overestimated grid-scale precipitation in most of the Yellow Sea regions. Since most hydrometeors were converted to

513 grid-scale precipitation in the Yellow Sea (Figure 11e), precipitation in the inland of the Korean
514 Peninsula was considerably less, as shown in Figure 10d. On the other hand, the MSKF run
515 realistically simulated low-level EPT, atmospheric stability, and hydrometeors in the Yellow Sea
516 (Figure 11c and f). Therefore, it reproduced strong convection and more hydrometeors over the
517 Cheong-ju region (127.9 °E), which resulted in a reasonable simulation of heavy precipitation by
518 the CPS and MPS.

519

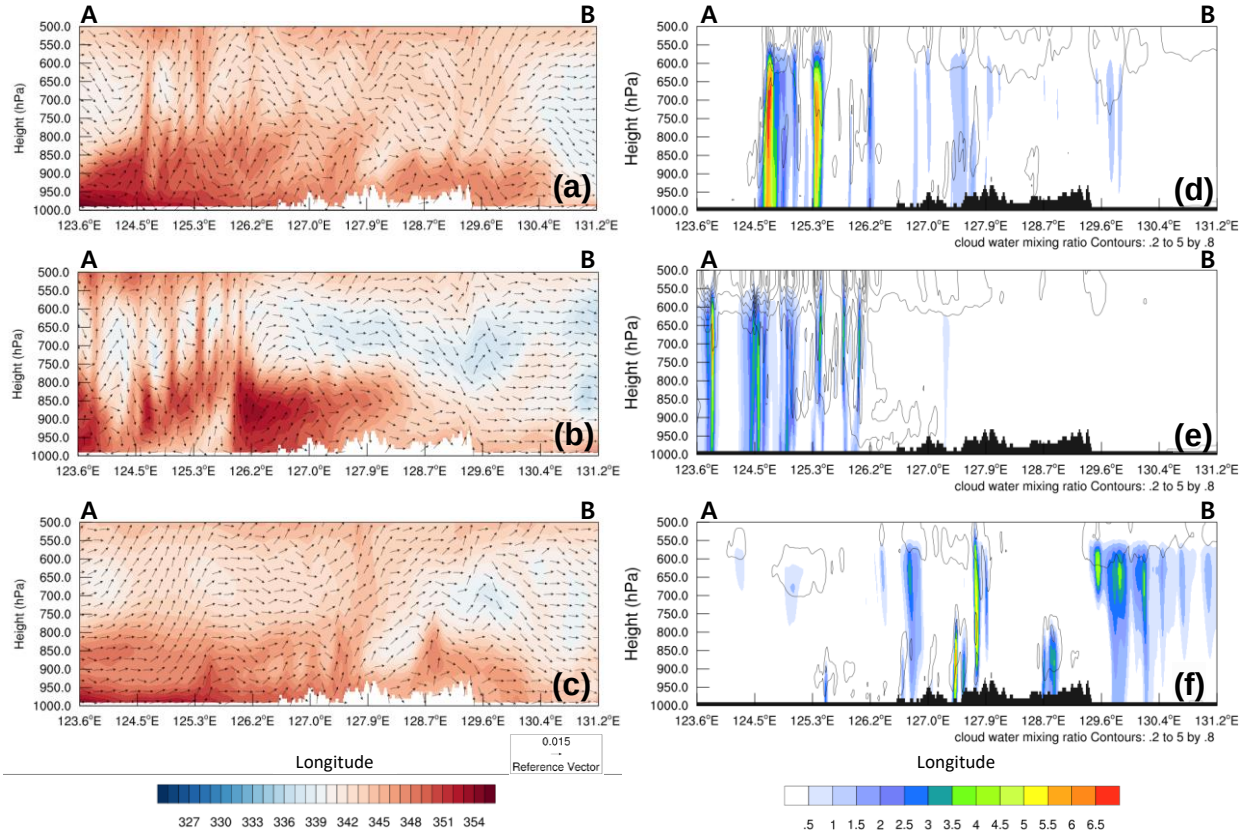


520

521 **Figure. 11**. Plots of the vertical cross-sections (AB in Figure 3b) of (a-c) equivalent potential
522 temperature (K, shaded) and wind (m $s^{-1}$, vector), and (d-f) cloud hydrometeors mixing ratio (g
523 $kg^{-1}$, shaded) and rain water mixing ratio (g $kg^{-1}$, contour) at 2100 UTC, 15 July 2017. Upper,
524 middle, and lower panels indicate the CTS, ENT, and MSKF runs, respectively. Cloud
525 hydrometeors are calculated by the summation of cloud water, ice, snow, and graupel.

526

## 4 Conclusion

This study investigated the impact of the scale-aware CPS across the gray-zone in the WRF model on a heavy precipitation event over the Korean Peninsula. We selected the KF and MSKF schemes as non-scale-aware CPS and scale-aware CPS, respectively. The MSKF scheme uses a scale-aware parameter modifying the CAPE timescale and the entrainment process of the KF scheme as a function of the horizontal grid spacing. The multi-nesting method is employed with four domains with 36, 12, 4, and 1.33 km horizontal resolutions to consider the gray-zone resolution.

According to our results, the KF runs (i.e., KF_D12 and KF runs) unreasonably overestimated precipitation in the Yellow Sea and distorted synoptic fields such as LLJs and moisture convergence. In the KF_D12 run, only the MPS resolved convective activities for the domains with high-resolution (i.e., 4 and 1.33 km) and overestimated grid-scale precipitation in the Yellow Sea because atmospheric instability is inadequately reduced. The CPS without scale-awareness (i.e., KF run) also caused the erroneous precipitation simulation due to the exaggeration of convection and distortion of the synoptic fields. Contrastingly, the MSKF run realistically simulated precipitation and synoptic fields. And, the sensitivity experiments for the scale-aware parameter (i.e., CTS and ENT runs) showed that the shorter CAPE timescale and decreased entrainment process of the KF scheme compared with those of the MSKF scheme led to the unreasonable fast development and exaggeration of convective activities, respectively. Additionally, the ENT run has a more significant error in simulated precipitation than the CTS run, suggesting that the enhanced entrainment process of the MSKF scheme contributes more to the improved simulation of heavy precipitation than the increased CAPE timescale. Consequently, the MSKF scheme with a scale-aware parameter realistically simulated

precipitation and synoptic fields by decreasing the subgrid-scale convection by the CPS and increasing the grid-scale convection by MPS as the horizontal resolution increases.

As the horizontal resolution of numerical models for weather forecasting has increased due to the remarkable advances in computing resources, more realistic grid-scale simulations are required. Studies have shown that (*Jeworrek et al.*, 2019; *Hong&Dudhia*, 2012) scale-aware physics schemes can improve the high-impact weather simulation when using very high-resolution numerical models. This study also improved the understanding of the scale-aware CPS role in heavy precipitation simulation at high-resolution. However, this study has some limitations. Only the KF-based CPSs in the WRF model and a heavy rainfall case in the Korean Peninsula are tested. Therefore, further experiments for the various scale-aware CPSs (e.g., scale-aware Grell-Freitas (*Grell&Freitas*, 2014) and gray-zone simplified Arakawa-Schubert (*Kwon&Hong*, 2017)) should be conducted for more heavy precipitation. We could also plan sensitivity tests using various combinations of the scale-aware CPSs and MPSs because the predictability of convective systems associated with heavy rainfall can depend on these combinations.

## Acknowledgments

This work was partially funded by the 2020 Republic of Korea Airforce Numerical Weather Prediction Research and Development Program, the development of Numerical Weather Prediction and Data Application Techniques, and the Ulsan National Institute of Science and Technology [Grant No. 1.210045.01].

## Data Availability Statement

The National Centers for Environmental Prediction Global Final Analysis (NCEP-FNL) data are available online (https://rda.ucar.edu/datasets/ds083.2/ and https://rda.ucar.edu/datasets/ds083.3/). IMERG was provided by the NASA Goddard Space Flight Center's IMERG and PPS teams, which develop and compute IMERG as a contribution to the GPM mission, and archived at the NASA GES DISC (https://disc.gsfc.nasa.gov/datasets/GPM_3IMERGHH_V06/summary) and online (https://gpm.nasa.gov/data/directory).

## Reference

Alapaty, K., Herwehe, J. A., Otte, T. L., Nolte, C. G., Bullock, O. R., Mallard, M. S., Kain, J. S., and Dudhia, J. (2012), Introducing subgrid-scale cloud feedbacks to radiation for regional meteorological and climate modeling, *39*(24), doi:https://doi.org/10.1029/2012GL054031.

Arakawa, A., Jung, J.-H., and Wu, C.-M. J. M. m. (2016), Multiscale modeling of the moist-convective atmosphere, *56*, 16.11-16.17.

Arakawa, A., Jung, J. H., and Wu, C. M. (2011), Toward unification of the multiscale modeling of the atmosphere, *Atmos. Chem. Phys.*, *11*(8), 3731-3742, doi:10.5194/acp-11-3731-2011.

Bechtold, P., Bazile, E., Guichard, F., Mascart, P., and Richard, E. J. Q. J. o. t. R. M. S. (2001), A mass-flux convection scheme for regional and global models, *127*(573), 869-886.

Bechtold, P., Koehler, M., Jung, T., Doblas-Reyes, F., Leutbecher, M., Rodwell, M. J., Vitart, F., Balsamo, G. J. Q. J. o. t. R. M. S. A. j. o. t. a. s., applied meteorology, and oceanography, p. (2008), Advances in simulating atmospheric variability with the ECMWF model: From synoptic to decadal time-scales, *134*(634), 1337-1351.

Bechtold, P., Semane, N., Lopez, P., Chaboureau, J.-P., Beljaars, A., and Bormann, N. J. J. o. A. S. (2014), Representing equilibrium and nonequilibrium convection in large-scale models, *71*(2), 734-753.

Bengtsson, L., and Körnich, H. (2016), Impact of a stochastic parametrization of cumulus convection, using cellular automata, in a mesoscale ensemble prediction system, *142*, 1150-1159.

Charles, M. E., Colle, B. A. J. W., and forecasting (2009), Verification of extratropical cyclones within the NCEP operational models. Part I: Analysis errors and short-term NAM and GFS forecasts, *24*(5), 1173-1190.

Cho, N.-S., and Lee, T.-Y. J. A.-P. J. o. A. S. (2006), A numerical study of multiple convection bands over the Korean peninsula, *42*(2), 87-105.

Choi, G., Kwon, W.-T., Boo, K.-O., and Cha, Y.-M. J. et al. (2008), Recent spatial and temporal changes in means and extreme events of temperature and precipitation across the Republic of Korea, *43*(5), 681-700.

Choi, Y., Lee, H., and Kwon, J. J. T. g. j. o. K. (2013), Recent change on frequency-magnitude of summer extreme rainfall events over the Republic of Korea, *47*(1), 83-97.

Chung, Y., Kim, H. J. A. Q., Atmosphere, and Health (2019), Observations on changes in Korean Changma rain associated with climate warming in 2017 and 2018, *12*(2), 197-215.

Davies, T., Cullen, M. J., Malcolm, A. J., Mawson, M., Staniforth, A., White, A., Wood, N. J. Q. J. o. t. R. M. S. A. j. o. t. a. s., applied meteorology, and oceanography, p. (2005), A new dynamical core for the Met Office's global and regional modelling of the atmosphere, *131*(608), 1759-1782.

Deng, A., Stauffer, D. R. J. J. o. a. m., and climatology (2006), On improving 4-km mesoscale model simulations, *45*(3), 361-381.

Dudhia, J. J. J. o. t. a. s. (1989), Numerical study of convection observed during the winter monsoon experiment using a mesoscale two-dimensional model, *46*(20), 3077-3107.

Dudhia, J. J. O. T. (2005), Chapter 8: Part II: Physics Options in MM5.

Emanuel, K. A., and Raymond, D. J. (1993), THE REPRESENTATION OF CUMULUS CONVECTION IN NUMERICAL MODELS %J Meteorological Monographs, *24*(46), 1-246, doi:10.1175/0065-9401-24.46.1.

Freitas, S. R., Grell, G. A., Molod, A., Thompson, M. A., Putman, W. M., Santos e Silva, C. M., and Souza, E. P. (2018), Assessing the Grell-Freitas Convection Parameterization in the NASA GEOS Modeling System, *10*(6), 1266-1289, doi:https://doi.org/10.1029/2017MS001251.

Fritsch, J. M., and Chappell, C. F. (1980), Numerical Prediction of Convectively Driven Mesoscale Pressure Systems. Part I: Convective Parameterization %J Journal of Atmospheric Sciences, *37*(8), 1722-1733, doi:10.1175/1520-0469(1980)037<1722:Npocdm>2.0.Co;2.

Fritsch, M. J., Chappell, C. F., and Hoxit, L. R. (1976), The Use of Large-Scale Budgets for Convective Parameterization %J Monthly Weather Review, *104*(11), 1408-1418, doi:10.1175/1520-0493(1976)104<1408:Tuolsb>2.0.Co;2.

Gerard, L. J. Q. J. o. t. R. M. S. A. j. o. t. a. s., applied meteorology, and oceanography, p. (2007), An integrated package for subgrid convection, clouds and precipitation compatible with meso-gamma scales, *133*(624), 711-730.

Grell, G. A., and Freitas, S. R. J. A. C. (2014), A scale and aerosol aware stochastic convective parameterization for weather and air quality modeling, *%J Atmospheric Chemistry Physics*, *14*(10), 5233-5250.

Gustafson, J. W. I., Ma, P. L., Xiao, H., Singh, B., Rasch, P. J., and Fast, J. D. J. J. o. G. R. A. (2013), The Separate Physics and Dynamics Experiment (SPADE) framework for determining resolution awareness: A case study of microphysics, *118*(16), 9258-9276.

Ha, K.-J., Park, S.-K., and Kim, K.-Y. (2005), On interannual characteristics of Climate Prediction Center merged analysis precipitation over the Korean peninsula during the summer monsoon season, *25*(1), 99-116, doi:https://doi.org/10.1002/joc.1116.

Han, J., Pan, H.-L. J. W., and Forecasting (2011), Revision of convection and vertical diffusion schemes in the NCEP Global Forecast System, *26*(4), 520-533.

Ho, C.-H., and Kang, I.-S. J. J. K. M. S. (1988), The variability of precipitation in Korea, *24*(1), 38-48.

Ho, C. H., Lee, J. Y., Ahn, M. H., and Lee, H. S. (2003), A sudden change in summer rainfall characteristics in Korea during the late 1970s, *Int J Climatol*, *23*(1), 117-128, doi:10.1002/joc.864.

Hong, S.-Y., and Dudhia, J. (2012), Next-Generation Numerical Weather Prediction: Bridging Parameterization, Explicit Clouds, and Large Eddies %J Bulletin of the American Meteorological Society, *93*(1), ES6-ES9, doi:10.1175/2011bams3224.1.

Hong, S.-Y., and Lee, J.-W. J. A. R. (2009), Assessment of the WRF model in reproducing a flash-flood heavy rainfall event over Korea, *93*(4), 818-831.

Hong, S.-Y., and Lim, J.-O. J. J. A.-P. J. o. A. S. (2006), The WRF single-moment 6-class microphysics scheme (WSM6), *42*(2), 129-151.

Hong, S.-Y., Noh, Y., and Dudhia, J. (2006), A New Vertical Diffusion Package with an Explicit Treatment of Entrainment Processes %J Monthly Weather Review, *134*(9), 2318-2341, doi:10.1175/mwr3199.1.

Huffman, G. J., Bolvin, D. T., Braithwaite, D., Hsu, K., Joyce, R., Xie, P., and Yoo, S.-H. J. A. T. B. D. V. (2015a), NASA global precipitation measurement (GPM) integrated multi-satellite retrievals for GPM (IMERG), *4*, 26.

Huffman, G. J., Bolvin, D. T., Nelkin, E. J., and Tan, J. J. N. G. C. (2015b), Integrated Multi-satellitE Retrievals for GPM (IMERG) technical documentation, *612*(47), 2019.

Jankov, I., Schultz, P. J., Anderson, C. J., and Koch, S. E. J. J. o. H. (2007), The impact of different physical parameterizations and their interactions on cold season QPF in the American River basin, *8*(5), 1141-1151.

Jeworrek, J., West, G., and Stull, R. (2019), Evaluation of Cumulus and Microphysics Parameterizations in WRF across the Convective Gray Zone %J Weather and Forecasting, *34*(4), 1097-1115, doi:10.1175/waf-d-18-0178.1.

Kain, J. S. J. J. o. a. m. (2004), The Kain–Fritsch convective parameterization: an update, *43*(1), 170-181.

Kang, I.-S., Ho, C.-H., and Min, K.-D. J. J. o. K. M. S. (1992), Long-range forecast of summer precipitation in Korea, *28*(3), 283-292.

Khairoutdinov, M., and Randall, D. J. J. o. A. S. (2006), High-resolution simulation of shallow-to-deep convection transition over land, *63*(12), 3421-3436.

Kim, C., Seo, M.-S., and Atmosphere, k. J. (2008), Change-Point in the Recent (1976-2005) Precipitation over South Korea, *18*(2), 113-122.

Kuang, Z., and Bretherton, C. S. J. J. o. t. A. S. (2006), A mass-flux scheme view of a high-resolution simulation of a transition from shallow to deep cumulus convection, *63*(7), 1895-1909.

Kwon, M., Jhun, J.-G., and Ha, K.-J. (2007), Decadal change in east Asian summer monsoon circulation in the mid-1990s, *34*(21), doi:https://doi.org/10.1029/2007GL031977.

Kwon, Y. C., and Hong, S.-Y. (2017), A Mass-Flux Cumulus Parameterization Scheme across Gray-Zone Resolutions %J Monthly Weather Review, *145*(2), 583-598, doi:10.1175/mwr-d-16-0034.1.

Lee, S.-H., Kim, E.-K., and Heo, I.-H. J. J. o. t. K. a. o. r. g. (2011a), A study on variability of extreme precipitation by basin in South Korea, *17*(5), 505-520.

Lee, S.-W., Lee, D.-K., and Chang, D.-E. J. A. i. A. S. (2011b), Impact of horizontal resolution and cumulus parameterization scheme on the simulation of heavy rainfall events over the Korean Peninsula, *28*(1), 1-15.

Lee, T.-Y., and Kim, Y.-H. (2007), Heavy Precipitation Systems over the Korean Peninsula and their Classification, *Asia-Pacific Journal of the Atmospheric Sciences*, *43*, 367-396.

Lin, C., and Arakawa, A. J. J. o. t. a. s. (1997), The macroscopic entrainment processes of simulated cumulus ensemble. Part I: Entrainment sources, *54*(8), 1027-1043.

Lin, Y., Zhao, M., Ming, Y., Golaz, J.-C., Donner, L. J., Klein, S. A., Ramaswamy, V., and Xie, S. (2013), Precipitation Partitioning, Tropical Clouds, and Intraseasonal Variability in GFDL AM2 %J Journal of Climate, *26*(15), 5453-5466, doi:10.1175/jcli-d-12-00442.1.

Lowrey, M. R. K., and Yang, Z.-L. (2008), Assessing the capability of a regional-scale weather model to simulate extreme precipitation patterns and flooding in central Texas, *%J Weather Forecasting*, *23*(6), 1102-1126.

Mishra, S. K., and Srinivasan, J. (2010), Sensitivity of the simulated precipitation to changes in convective relaxation time scale, paper presented at Annales Geophysicae, Copernicus GmbH.

Mlawer, E. J., Taubman, S. J., Brown, P. D., Iacono, M. J., and Clough, S. A. (1997), Radiative transfer for inhomogeneous atmospheres: RRTM, a validated correlated-k model for the longwave, *102*(D14), 16663-16682, doi:https://doi.org/10.1029/97JD00237.

MOIS (2019), Ministry of Interior and Safety (MOIS). https://www.mois.go.kr/frt/a01/frtMain.do.

Molinari, J., and Dudek, M. J. M. W. R. (1992), Parameterization of convective precipitation in mesoscale numerical models: A critical review, *120*(2), 326-344.

Mun, T., Park, C., Kim, G., and Cha, D.-H. (2019), Long-term Variability of Summer Heavy Rainfall in the Seoul Metropolitan Area, *14*(4), 209-219.

Noh, Y., Cheon, W. G., Hong, S. Y., and Raasch, S. (2003), Improvement of the K-profile Model for the Planetary Boundary Layer based on Large Eddy Simulation Data, *Boundary-Layer Meteorology*, *107*(2), 401-427, doi:10.1023/A:1022146015946.

Olson, D. A., Junker, N. W., and Korty, B. (1995), Evaluation of 33 Years of Quantitative Precipitation Forecasting at the NMC %J Weather and Forecasting, *10*(3), 498-511, doi:10.1175/1520-0434(1995)010<0498:Eoyoqp>2.0.Co;2.

Park, C.-Y., Moon, J.-Y., Cha, E.-J., Yun, W.-T., and Choi, Y.-E. J. J. o. t. K. G. S. (2008), Recent changes in summer precipitation characteristics over South Korea, *43*(3), 324-336.

Prein, A. F., Langhans, W., Fosser, G., Ferrone, A., Ban, N., Goergen, K., Keller, M., Tölle, M., Gutjahr, O., and Feser, F. J. R. o. g. (2015), A review on regional convection-permitting climate modeling: Demonstrations, prospects, and challenges, *53*(2), 323-361.

Saito, K., Fujita, T., Yamada, Y., Ishida, J.-i., Kumagai, Y., Aranami, K., Ohmori, S., Nagasawa, R., Kumagai, S., and Muroi, C. J. M. W. R. (2006), The operational JMA nonhydrostatic mesoscale model, *134*(4), 1266-1298.

709 Shin, C.-S., and Lee, T.-Y. J. J. o. t. M. S. o. J. S. I. (2005), Development mechanisms for the heavy rainfalls of 6-7
710 August 2002 over the middle of the Korean Peninsula, *83*(5), 683-709.
711 Sims, A. P., Alapaty, K., and Raman, S. J. M. w. r. (2017), Sensitivities of summertime mesoscale circulations in the
712 coastal carolinas to modifications of the kain–fritsch cumulus parameterization, *145*(11), 4381-4399.
713 Sun, J., and Lee, T.-Y. J. J. o. t. M. S. o. J. S. I. (2002), A numerical study of an intense quasi-stationary convection
714 band over the Korean Peninsula, *80*(5), 1221-1245.
715 Tokioka, T., Yamazaki, K., Kitoh, A., and Ose, T. J. J. o. t. M. S. o. J. S. I. (1988), The equatorial 30-60 day
716 oscillation and the Arakawa-Schubert penetrative cumulus parameterization, *66*(6), 883-901.
717 Wang, H., Zhang, M., and Liu, M. J. J. o. A. M. S. (2006), Influence of Moist Schemes in MM5 on the Uncertainties
718 of "03· 7" Heavy Rainfall Numerical simulation, *17*(3), 346-353.
719 Wang, S., Sobel, A. H., Zhang, F., Sun, Y. Q., Yue, Y., and Zhou, L. J. J. o. C. (2015), Regional simulation of the
720 October and November MJO events observed during the CINDY/DYNAMO field campaign at gray zone resolution,
721 *28*(6), 2097-2119.
722 Wang, W., and Seaman, N. L. (1997), A Comparison Study of Convective Parameterization Schemes in a Mesoscale
723 Model %J Monthly Weather Review, *125*(2), 252-278, doi:10.1175/1520-0493(1997)125<0252:Acsocp>2.0.Co;2.
724 Weisman, M. L., Skamarock, W. C., and Klemp, J. B. J. M. W. R. (1997), The resolution dependence of explicitly
725 modeled convective systems, *125*(4), 527-548.
726 Yang, M.-J., Chien, F.-C., Cheng, M.-D. J. T., Atmospheric, and Sciences, O. (2000), Precipitation Parameterization
727 in a Simulated Mei-Yu Front, *11*(2), 393-422.
728 Yu, X., Lee, T.-Y. J. T. A. D. M., and Oceanography (2010), Role of convective parameterization in simulations of
729 a convection band at grey-zone resolutions, *62*(5), 617-632.
730 Zheng, Y., Alapaty, K., Herwehe, J. A., Del Genio, A. D., and Niyogi, D. J. M. W. R. (2016), Improving high-
731 resolution weather forecasts using the Weather Research and Forecasting (WRF) Model with an updated Kain–
732 Fritsch scheme, *144*(3), 833-860.

733